DOI: 10.19884/j.1672-5220.202304007

Performance Evaluation of a Photovoltaic Module-Driven van der Waals Heterostructure-Based Thermionic Refrigerator

LU Zhen, HUANG Yuewu*
College of Environmental Science and Engineering, Donghua University, Shanghai 201620, China

Abstract: For developing an efficient solar cooling technology, a novel coupled system comprising a photovoltaic (PV) module and a van der Waals heterostructure (vdWH)-based thermionic refrigerator (TIR) is established. With full consideration of internal and external irreversibility, the theoretical model of the coupled system is constructed, and mathematical expressions for the key performance indicators are derived. On this basis, the general properties of the coupled system are investigated, and the voltage region permitting the system to operate is determined. According to the calculations, the maximum refrigerating capacity and the maximum coefficient of performance (COP) are 75.88 W and 0.49, respectively. Furthermore, sensitivity analyses are conducted to derive the regularity and magnitude of the impacts of critical parameters on the overall performance of the coupled system, including solar irradiance, effective Schottky barrier height, inter-layer thermal resistance, external thermal resistance, heat leakage thermal resistance and hot reservoir temperature. The obtained outcomes may contribute to the design and operation of practical coupled systems.

Key words: photovoltaic (PV) module; thermionic refrigerator (TIR); van der Waals heterostructure (vdWH); coupling characteristic; sensitivity assessment
CLC number: TK511.3 **Document code**: A
Article ID: 1672-5220(2024)02-0146-10

Open Science Identity (OSID)

0 Introduction

Currently, fossil fuels remain the major component of global energy consumption, but the worldwide problems of environmental pollution and energy shortages are also becoming more prominent[1-2]. Against this backdrop, there is a burgeoning focus on renewable energy sources such as solar energy, geothermal energy, wind energy and wave energy, accelerating the construction of a low-carbon energy structure[3]. Amongst them, solar energy has outstanding advantages in terms of wide distribution, direct convertibility and cleanliness, which makes it a potential candidate for solving global energy problems[4-5].

To make stable and efficient use of solar energy, researchers have proposed various means of application[6]. Solar cooling is one of the promising technologies that can tackle the growing demand for cooling[7]. Depending on the technical route, it can be divided into solar electric cooling and solar thermal cooling technologies. The former uses solar-generated electricity to power the refrigerator, while the latter collects solar energy as a heat source and then applies it to drive the refrigeration devices[8-9]. Currently, solar electric cooling technology has been extensively and intensively investigated. For example, Dai et al.[10] investigated the system performance of a solar cell-powered thermoelectric cooler based on theories and experiments and found that the system could effectively keep the temperature in a refrigerator at 5−10 ℃. Cheng et al.[11] applied a solar-powered thermoelectric cooling system to the thermal management of the building. The system achieved a temperature difference of 16.2 ℃ during steady operation. Zhao et al.[12] evaluated the performance of a thermoelectric refrigerator powered by dye-sensitized solar cells. The outcomes indicated that the system's coefficient of performance (COP) under optimal conditions was 0.8. Long et al.[13] designed a solar cooling installation comprising a thermally regenerative electrochemical refrigerator and a photovoltaic (PV) module, in which the impact of various factors on the system properties was analyzed. Liao et al.[14] investigated the performance of a thermoelectric cooling system driven by a PV module and obtained an optimized system efficiency of 13.9%.

A thermionic refrigerator (TIR) is a solid-state refrigeration unit, originally conceived by Mahan[15] in the 1990s. Several investigations have demonstrated that the theoretical efficiency of TIR is superior to that of thermoelectric devices[16-17]. However, its cooling at room temperature is still challenging due to the limitations of the electrode material[18-19]. To fundamentally overcome this limitation, numerous innovative thermionic refrigeration technologies have gradually emerged. For instance, Shakouri et al.[20] first proposed using a heterostructure in the device to realize thermionic

Received date: 2023-04-11
* Correspondence should be addressed to HUANG Yuewu, email: huangyuewu@dhu.edu.cn
Citation: LU Z, HUANG Y W. Performance evaluation of a photovoltaic module-driven van der Waals heterostructure-based thermionic refrigerator[J]. *Journal of Donghua University (English Edition)*, 2024, 41(2): 146-155.

emission. Although this method could effectively diminish the work function, the cooling efficiency was significantly hampered by the irreversible thermal conductivity between two electrodes. Mahan et al.[21] optimized the thermionic refrigerator based on a multi-layer barrier structure and analyzed the performance in detail. Fan et al.[22] constructed a SiGeC/Si superlattice thermionic refrigerator with experimentally measured cooling temperature differences of 2.80 K and 6.90 K obtained at 298.15 K and 373.15 K, respectively. With advances in materials and systems, van der Waals heterostructures (vdWHs) comprising multilayer transition metal dichalcogenides (TMDs) were applied to thermionic devices[23-24]. Wang et al.[25] used the first principle to investigate the properties of thermionic devices composed of vdWHs. Results indicated that the system exhibited excellent cooling performance when the temperature exceeded 450 K. Qiu et al.[26] designed and numerically analyzed a theoretical model of a vdWHs thermionic refrigerator, revealing the optimal operating region for the entire apparatus. Liang et al.[27] established a thermionic energy conversion device based on vdWHs. When utilized as a refrigerator, the device achieved a cooling efficiency of 21.94% of the Carnot efficiency under ideal conditions. The vdWH has great potential in the field of thermionic cooling, as it can effectively exploit the low thermal conductivity of TMDs and significantly improve the thermionic emission process of the device, making efficient cooling of thermionic refrigerators at low and medium temperatures feasible[27-29].

The synthesis of previous research revealed that investigations focusing on hybrid solar cooling systems with the PV module and the vdWH thermionic refrigerator are not available. Targeted investigation can simulate the performance characteristics of this specific coupled system and provide new insights into the development and utilization of solar electric cooling systems.

Thus, to bridge this investigation gap, this work integrates a vdWH thermionic refrigerator into a PV module system that exploits the electricity generated by the PV module for cooling production. A comprehensive theoretical model of the proposed system is established, and analytical formulas for the refrigerating capacity and the COP are derived. On this basis, the coupling properties and the cooling capacity of the system are investigated. In addition, an extensive parametric analysis is undertaken to evaluate the impact of several critical parameters on the installation's performance.

1 System Description

Figure 1 schematically portrays the proposed coupled system, mainly consisting of a PV module and a vdWH thermionic refrigerator.

When sunlight irradiates the PV module surface, partial solar energy is converted into electricity and employed directly to power the subordinate thermionic refrigerator for cooling. In this coupled system, I_{PV} stands for the current of the PV module; T_{PV} is the PV module's working temperature; Q_C and Q_H represent the heat transfer at the cathode and the anode of the refrigerator, respectively; J_C and J_H represent the thermionic current densities emitted from the cathode and the anode surfaces, respectively; Q_I is the heat transfer between the graphene-TMD interfaces and within the TMD layers; T_1 and T_2 are the temperatures of the anode and the cathode of TIR, respectively; T_H and T_C are the hot reservoir temperature and the cold reservoir temperature, respectively. As a refrigeration device, $T_1>T_H>T_C>T_2$.

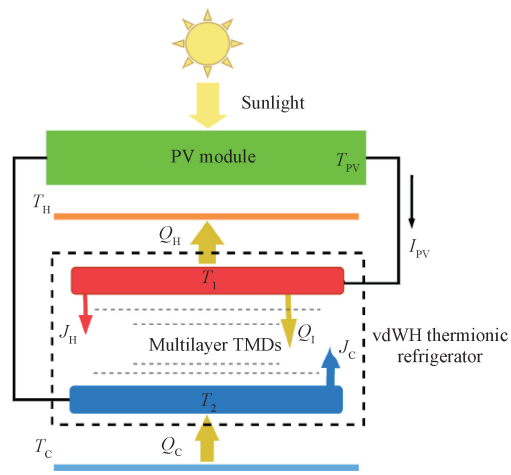

Fig. 1 Schematic diagram of coupled system

In the following, the two subsystems and the coupled system are depicted and mathematically analyzed in turn. And the next sensible hypotheses are applied to simplify the modeling intricacies.

1) The coupled system operates under steady-state conditions[30].

2) The incident wavelength of sunlight is fully utilized[31].

3) The PV module is regarded as a current source parallel to the diode and dependent on irradiance[32].

4) The influence of lateral momentum non-conservation on the thermionic refrigerator is neglected[27].

1.1 PV module

As sunlight irradiates the PV module, new electron-hole pairs are generated. Owing to the internal electric field, electrons move from the P zone to the N zone while holes are pushed towards the P zone, creating a new potential difference. With the PV effect, a continuous current flows through the circuit when the external circuit is connected[33-34].

Figure 2 depicts the equivalent circuit of the PV module, where V_{PV} denotes the PV module's output voltage; I_{PV}, I_0 and I_{ph} are the output current, reverse current and photocurrent of the PV module, respectively; R_s and R_{sh} stand for the intrinsic series resistance and

shunt resistance, respectively.

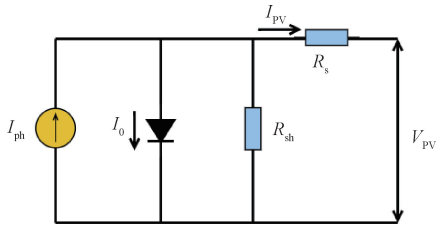

Fig. 2 Equivalent circuit of PV module

Depending on Ref. [35], the photocurrent I_{ph} is obtained by

$$I_{ph} = \frac{G}{G_{ref}}[I_{ph,\,ref} + \mu(T_{PV} - T_{ref})], \tag{1}$$

where G indicates the solar irradiance; G_{ref} and T_{ref} represent reference solar irradiance and temperature, respectively; $I_{ph,\,ref}$ is the short-circuit current under the reference conditions; μ refers to the temperature correlation coefficient.

The reverse saturation current I_r can be expressed as

$$I_r = I_{r,\,ref}\left(\frac{T_{PV}}{T_{ref}}\right)^3 \exp\left[\frac{E_g q}{K_b m}\left(\frac{1}{T_{ref}} - \frac{1}{T_{PV}}\right)\right], \tag{2}$$

where q represents the charge of an electron; E_g is the energy gap of the silicon crystals; m is the diode ideality factor; K_b is the Boltzmann constant; $I_{r,\,ref}$ is the reverse saturation current at T_{ref}.

The current-voltage characteristics of the PV module can be expressed as[32]

$$I_{PV} = n_p I_{ph} - n_p I_r\left\{\exp\left[\frac{q(V_{PV} + I_{PV}R_s)}{mK_b T_{PV} n_s}\right] - 1\right\}, \tag{3}$$

where n_s and n_p are the amounts of cells connected in series and parallel, respectively.

Thus, the output power of the PV module under reference conditions $P_{PV,\,ref}$ is given by[36]

$$P_{PV,\,ref} = V_{PV}I_{PV} = V_{PV}n_p I_{ph} - V_{PV}n_p I_r\left\{\exp\left[\frac{q(V_{PV} + I_{PV}R_s)}{mK_b T_{PV} n_s}\right] - 1\right\}. \tag{4}$$

Considering the significant impact of variations in working temperature on the PV module's performance, the actual output power of the PV module P_{PV} is[37]

$$P_{PV} = P_{PV,\,ref}[1 - \alpha(T_{PV} - T_{ref})], \tag{5}$$

where α is the empirical rate of decline in the output power, and $\alpha = [1.069 - 0.00469(T_{PV} - 273.15)]\%$.

Meanwhile, the efficiency of the PV module η_{PV} can be calculated as

$$\eta_{PV} = \frac{P_{PV}}{GA_{PV}}, \tag{6}$$

where A_{PV} is the surface area of the PV module.

1.2 TIR based on vdWHs

The efficient solid-state thermionic refrigerator based on vdWHs is composed of graphene electrodes and multi-layer TMDs. In the absence of the bias voltage, the hot electrode of TIR has a larger potential energy, and electrons flow more readily from the hot electrode to the cold electrode. When a sufficiently large reverse voltage is exerted on the cold electrode, its potential energy increases, allowing electrons to flow from the cold electrode to the hot electrode. The flow of electrons removes heat from the cold electrode and thus cooling is achieved.

Externally, TIR transfers heat between the electrodes and their corresponding reservoirs. The heat released by the graphene anode Q_H and the heat absorbed by the graphene cathode Q_C can be respectively calculated as[38]

$$Q_H = K_1 A_1(T_1 - T_H), \tag{7}$$

$$Q_C = K_2 A_2(T_C - T_2), \tag{8}$$

where K_1, K_2, A_1 and A_2 refer to the effective heat transfer coefficients and areas between the anode and the cathode with their corresponding external reservoirs, respectively.

For graphene electrodes, the thermionic current densities emitted from the anode and cathode surfaces after applying the bias voltage V_{TIR} are[39]

$$J_H = \beta T_1^3 \exp\left(-\frac{q\varphi + qV_{TIR}}{K_b T_1}\right), \tag{9}$$

$$J_C = \beta T_2^3 \exp\left(-\frac{q\varphi}{K_b T_2}\right), \tag{10}$$

where $\beta = 1.158 \times 10^{-2}\,\mathrm{A/(cm^2 \cdot K^3)}$; φ is the effective Schottky barrier height. $\varphi = \varphi_0 E_F/q$, where E_F is the intrinsic Fermi level; φ_0 is the Schottky barrier height at zero bias.

Combining Eqs. (9) and (10), the net current density J is obtained by

$$J = J_C - J_H = \beta T_2^3 \exp\left(-\frac{q\varphi}{K_b T_2}\right) - \beta T_1^3 \exp\left(-\frac{q\varphi + qV_{TIR}}{K_b T_1}\right). \tag{11}$$

The input power of TIR P_{TIR} can be obtained as

$$P_{TIR} = JV_{TIR}A_3, \tag{12}$$

where A_3 denotes the effective area between electrodes.

The transport of electrons between electrodes causes energy transfer, and the related heat can be given by[27]

$$\dot{Q}_H = (\varphi + V_{TIR} + 3K_b T_2/q)A_3 J_C - (\varphi + V_{TIR} + 3K_b T_1/q)A_3 J_H, \tag{13}$$

$$\dot{Q}_C = (\varphi + 3K_b T_2/q)A_3 J_C - (\varphi + 3K_b T_1/q)A_3 J_H, \tag{14}$$

where $\dot{Q}_H$ and $\dot{Q}_C$ represent the heat transfer at the anode and the cathode due to the transport of electrons, respectively.

Besides, heat transfer Q_I exists between the graphene-TMD interfaces and within the TMD layers, which depends mainly on the inter-layer thermal resistance R_I. According to Ref. [19], it can be written as

$$Q_I = A_3(T_1 - T_2)/R_I. \quad (15)$$

For calculation convenience, Eqs. (7) and (8) can also be formulated in terms of thermal resistance as

$$Q_H = A_1(T_1 - T_H)/R_H, \quad (16)$$

$$Q_C = A_2(T_C - T_2)/R_C, \quad (17)$$

where R_H is the thermal resistance between the anode and the hot reservoir; R_C is the thermal resistance between the cathode and the cold reservoir.

Combining Eqs. (13)−(17), the energy balance equations of the two electrodes at the steady state are

$$A_1(T_1 - T_H)/R_H = (\varphi + V_{TIR} + 3K_bT_2/q)A_3J_C - (\varphi + V_{TIR} + 3K_bT_1/q)A_3J_H - A_3(T_1 - T_2)/R_I, \quad (18)$$

$$A_2(T_C - T_2)/R_C = (\varphi + 3K_bT_2/q)A_3J_C - (\varphi + 3K_bT_1/q)A_3J_H - A_3(T_1 - T_2)/R_I. \quad (19)$$

1.3 Solar-driven thermionic refrigeration system

Considering heat leakage between the cold reservoir and the hot reservoir, i.e. $Q_L = A_4(T_H - T_C)/R_L$, the refrigerating capacity of the device is given by

$$Q_r = A_2(T_C - T_2)/R_C - A_4(T_H - T_C)/R_L, \quad (20)$$

where A_4 and R_L are the heat transfer area and thermal resistance between the cold reservoir and the hot reservoir, respectively.

As we set $Q_r = 0$, the critical voltage value V_{0,Q_r} for the cooling rate being zero can be obtained, which can be given by

$$V_{0,Q_r} = \frac{K_bT_1}{q}\ln\left\{\frac{A_3\beta T_1^3(\varphi + 3K_bT_1/q)\exp[q\varphi(T_1 - T_2)/(K_bT_1T_2)]}{A_3\beta T_2^3(\varphi + 3K_bT_2/q) - (Q_I + Q_L)\exp[q\varphi/(K_bT_2)]}\right\}. \quad (21)$$

Since the power required for TIR at the bottom of the system is entirely supplied by the PV module, the coupling condition of the system is

$$P_{PV} = P_{TIR}. \quad (22)$$

The COP denoted by C_{OP} of the system is calculated as

$$C_{OP} = \frac{Q_r}{P_{PV}} = \frac{A_2(T_C - T_2)/R_C - A_4(T_H - T_C)/R_L}{V_{PV}I_{PV}[1 - \alpha(T_{PV} - T_{ref})]}. \quad (23)$$

Furthermore, according to Eqs. (5), (11), (12) and (22), the relationship between V_{PV} and V_{TIR} satisfies

$$V_{PV}I_{PV}[1 - \alpha(T_{PV} - T_{ref})] = V_{TIR}A_3\left[\beta T_2^3\exp\left(-\frac{q\varphi}{K_bT_2}\right) - \beta T_1^3\exp\left(-\frac{q\varphi + qV_{TIR}}{K_bT_1}\right)\right]. \quad (24)$$

Table 1 Default parameters used in coupled system

Parameter	Value	Parameter	Value
T_{PV} /K	345[35]	T_C /K	260[38]
φ /V	0.05[40]	T_H /K	300[38]
G/(W/m^2)	800	R_I /(K·m^2/W)	50.15×10^{-7}[26]
T_{ref} /K	300	R_H /(K·m^2/W)	10^{-6}[26]
G_{ref} /(W/m^2)	1 000	R_C /(K·m^2/W)	10^{-6}
$I_{ph,ref}$ /A	9.43	R_L /(K·m^2/W)	1.1×10^{-3}[24]
$I_{r,ref}$ /A	1.18×10^{-7}	n_s	60
μ/(A/K)	3×10^{-3}	n_p	1
E_g /eV	1.12[35]	m	1.23

2 Model Validation

Relevant experimental reports on this coupled system are not yet available, but previous studies have individually assessed the PV module. Thus, the PV module is verified in contrast to the experimental results in the existing literature. Figure 3(a) compares the modeling results with the experimental results from practical Suniva PV modules[41]. The relevant data are measured at a temperature of 298.15 K and a solar irradiance of 800 W·m^2. Evidently, the trend of the present model's I_{PV}-V_{PV} curve is consistent with the practical PV module, and the data between them are in good agreement. Moreover, according to experimental data from Sachenko et al.[42], the η_{PV}-T_{PV} curve of the current PV model is validated and compared. The experiment employs a solar radiation simulator to produce an irradiance of 1 000 W·m^2 with the AM (air mass) 1.5 G spectrum. A VPF-100 cryostat is placed in the experimental setup to guarantee temperature stability within the measurement temperature range. As can be observed in Fig. 3(b), the efficiency of each PV module decreases monotonically as the working temperature grows, and the modeling results agree well with the experimental results.

To more specifically contrast the experimental results with the modeling results, the average relative error formula $E_r = \frac{1}{n}\sum_{i=1}^{n}|(X_{mod,i} - X_{exp,i})/X_{exp,i}| \times 100\%$ is introduced, where $X_{exp,i}$ and $X_{mod,i}$ represent the experimental value and the simulated value, respectively[43]. The results indicate that the average relative errors are 3.63% (Fig. 3(a)) and 1.75% (Fig. 3(b)), respectively. The great consistency between the model and experimental results demonstrates that the established model is valid and dependable.

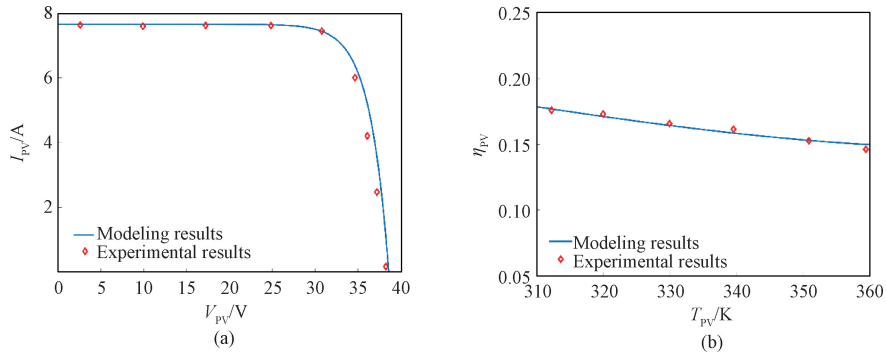

Fig. 3 Model validation: (a) comparison of I_{PV}-V_{PV} relationship between modeling results and experimental results from Ref. [41]; (b) comparison of η_{PV}-T_{PV} relationship between modeling results and experimental results from Ref. [42]

3 Generic Performance Features

To elucidate the coupling characteristics of the proposed system, its generic performance features in the standard state are fully investigated and evaluated. The parameters required to numerically solve the coupled system are listed in Table 1, and the associated solution flow is illustrated in Fig. 4.

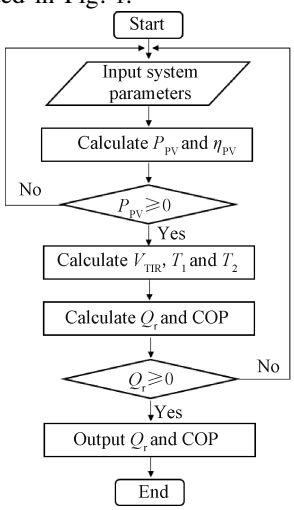

Fig. 4 Flow chart for solving the coupled system

Figure 5 depicts the curves of P_{TIR} and V_{TIR} of TIR as a function of V_{PV}. In Fig. 5, $P_{TIR,max}$ and V_p are the maximum input power and its corresponding PV module voltage, respectively; V_{0,Q_r} is the TIR voltage when the refrigerating capacity is zero; V_{lb} and V_{ub} represent the lower and upper voltages permitted to operate the coupled system. It can be observed that both P_{TIR} and V_{TIR} increase and then decrease as V_{PV} grows. There is an optimal voltage V_p that allows P_{TIR} and V_{TIR} to achieve their maximum values. In fact, V_{TIR} is proportional to P_{TIR}, and P_{TIR} is tightly associated with the working voltage of the PV module. When V_{PV} is lower than the critical value V_p, the working current of the PV module rises as V_{PV} grows, leading to an increase in input power. As V_{PV} exceeds V_p, the operating current of the PV model decreases because the positive bias voltage at the PN junction approaches the photogenerated electric potential, leading to a reduction in P_{TIR}. In addition, based on Eq. (21), the voltage V_{0,Q_r} at $Q_r = 0$ can be obtained, as well as the corresponding lower limit V_{lb} and upper limit V_{ub} of V_{PV} permitted to operate the coupled system. Thus, the operating voltage range of the system should be located in $[V_{lb}, V_{ub}]$ for cooling purposes.

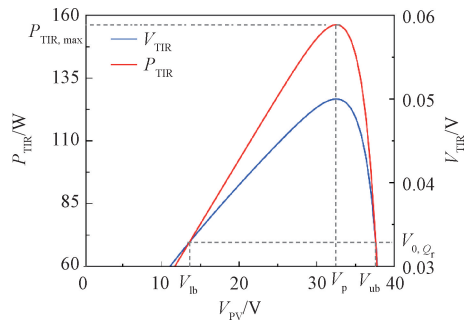

Fig. 5 Curves of P_{TIR} and V_{TIR} versus V_{PV}

Furthermore, Fig. 6 illustrates the effect of V_{PV} on Q_r and C_{OP} of the coupled system. In Fig. 6, $Q_{r,max}$ and $C_{OP,max}$ are the maximum values of Q_r and C_{OP}; V_m is the operating working voltage corresponding to $Q_{r,max}$ and $C_{OP,max}$. Clearly, both Q_r and C_{OP} first rise and then fall with increasing V_{PV} within the permitted operating voltage range. At $V_{PV} = 32.49$ V, Q_r reaches its maximum value $Q_{r,max}$ of 75.88 W, and C_{OP} achieves its maximum value $C_{OP,max}$ of 0.49. It can be noticed that the voltages that make Q_r and C_{OP} reach their maximum values are identical.

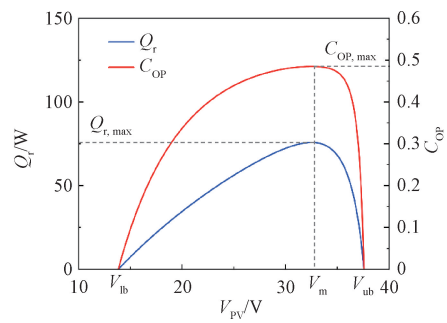

Fig. 6 Curves of Q_r and C_{OP} versus V_{PV}

4 Results and Discussion

According to the above model, the performance of the coupled system is profoundly affected by various parameters, mainly including solar irradiance G, effective Schottky barrier height φ, inter-layer thermal resistance R_I, external thermal resistance R_E, heat leakage thermal resistance R_L, and hot reservoir temperature T_H. Thus, integrated sensitivity assessments are performed to explore how they affect the whole performance. Moreover, the parameters in Table 1 are considered to be the default parameters of the coupled system unless specifically indicated.

4.1 Effects of solar irradiance

As an essential parameter of the coupled system, the variation in solar irradiance G affects the overall amount of solar energy entering the system, and therefore its impact on the properties needs to be evaluated. Figure 7 presents the integrated influences of G and V_{PV} on the refrigerating capacity Q_r and C_{OP}. It can be seen that when G holds constant, Q_r and C_{OP} both initially increase and then decrease as V_{PV} increases, and when V_{PV} remains constant, the coupled system's performance is considerably improved with increasing G. This is consistent with the physical significance of G. A larger G represents more energy entering the mixed unit, which means that more electrical energy is applied to drive the thermionic refrigerator for cooling. Thus, the capacity of the coupled system is enhanced. Additionally, it is notable that Q_r is more sensitive to variations of G compared to C_{OP}. For example, when G rises from 700 W/m^2 to 1 000 W/m^2 at V_{PV} = 32.49 V, Q_r increases from 61.12 W to 97.65 W, while C_{OP} only increases from 0.45 to 0.49. In general, the enhancement of G is salutary to the coupled system's integral capabilities. G is intimately linked to parameters such as latitude, weather and season, and numerous innovative technologies have been investigated to obtain more incident solar energy[44].

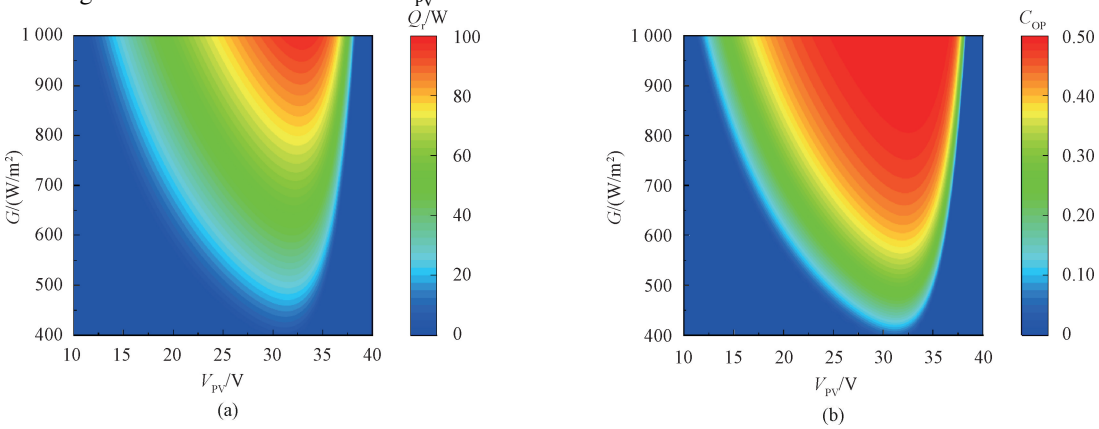

Fig. 7 Combined effects of G and V_{PV} on (a) Q_r; (b) C_{OP}

4.2 Effects of effective Schottky barrier height

Effective Schottky barrier height φ characterizes the lowest energy needed for electrons to escape from the surface of the TIR electrode. Figure 8 illustrates the combined influences of φ and V_{PV} on Q_r and C_{OP}. It can be observed that the coupled system performance is sensitive to φ. When φ decreases from 0.06 to 0.03 at V_{PV} = 30.00 V, Q_r increases from 50.21 W to 74.25 W, and C_{OP} increases from 0.33 to 0.49. This is because the reduction in φ makes electrons easier to escape from the TIR electrodes, leading to a higher electron emission current density, and this means that the energy flux of electron emission is significantly enhanced.

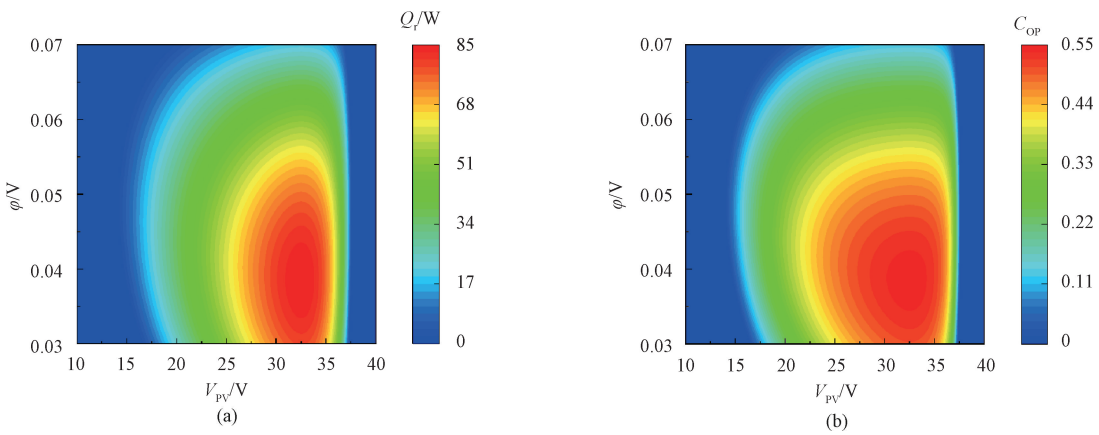

Fig. 8 Combined effects of φ and V_{PV} on (a) Q_r; (b) C_{OP}

Meanwhile, for a fixed φ, Q_r and C_{OP} always increase and then decrease as V_{PV} grows. Choosing materials with a lower φ tends to make the system perform better, and the pursuit of emitting materials with a lower φ has been a topical issue in the realm of thermionic emission over recent years.

4.3 Effects of inter-layer thermal resistance

The inter-layer thermal resistance R_I is a critical parameter in determining the property of TIR, which further influences the overall capability of the system. Figure 9 illustrates the performance characteristics of the proposed system within a range of R_I. It can be noticed that as R_I increases, both $Q_{r,\max}$ and $C_{OP,\max}$ first rise sharply and then remain almost constant. When R_I is low, the system's performance is very sensitive to variations in R_I. For example, as R_I enlarges from 4×10^{-6} K·m^2/W to 2×10^{-5} K·m^2/W, $Q_{r,\max}$ increases from 39.09 W to 210.91 W and $C_{OP,\max}$ grows from 0.25 to 1.58. The potential mechanism for this phenomenon can be explained as follows. For solid-state thermionic devices, the primary disadvantage is that the heat transfer caused by lattice vibrations in the semiconductor potential barrier layers results in a loss of cooling capacity. The lower the inter-layer thermal resistance is, the greater the loss will be. When R_I increases sufficiently, this heat transfer is significantly inhibited and the influence on cooling performance becomes weaker. From the analysis above, R_I is the critical parameter that has a significant impact on system performance and its value needs to be enlarged within reasonable limits. The number of TMD layers and the inherent thermal conductivity of the TMDs are the major factors in determining R_I. To strengthen the cooling capacity, vdWHs with the reasonable thickness and low cross-sectional thermal conductivity are required in the designs.

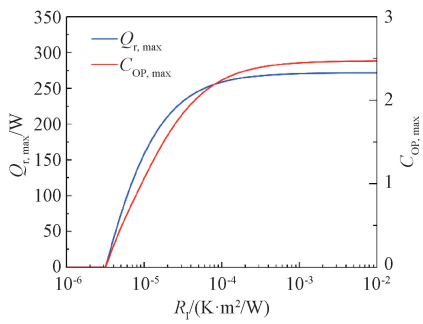

Fig. 9 Curves of $Q_{r,\max}$ and $C_{OP,\max}$ versus R_I

4.4 Effects of external thermal resistance

As can be seen from Eqs. (18) and (19) that external thermal resistance R_E is tightly related to the coupled system performance, and the impact of its variation on performance needs to be investigated. For the convenience of discussion, it can be noted that $R_H = R_C = R_E$. Figure 10 presents the $Q_{r,\max}$ and $C_{OP,\max}$ of the coupled system at different R_E. Obviously, both $Q_{r,\max}$ and $C_{OP,\max}$ decrease monotonically as R_E increases. This is because the increase in R_E weakens the heat transfer between the graphene electrode and the external reservoir and therefore deteriorates the performance of the coupled system. When $R_E = 1.5\times10^{-6}$ K·m^2/W, $Q_{r,\max}$ and $C_{OP,\max}$ are 48.71 W and 0.31, respectively. When $R_E \to 0$, i.e., $K_1A_1 = K_2A_2 \to \infty$, $T_1 = T_H$, $T_2 = T_C$, the irreversible heat transfer between the thermionic refrigerator and the outside is ignored, and $Q_{r,\max}$ and $C_{OP,\max}$ can rise to about 179.92 W and 1.15, respectively. By comparing the non-ideal and ideal cases, it is clear that the influence of R_E on the properties of the coupled system is significant. Consequently, R_E ought to be as low as feasible, otherwise, the capacity of the system will be reduced.

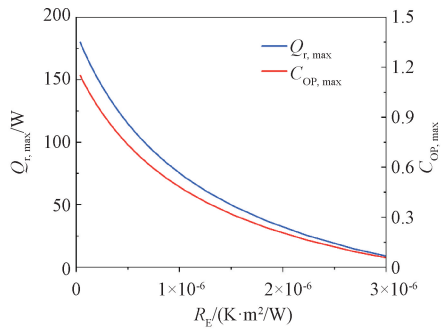

Fig. 10 Curves of $Q_{r,\max}$ and $C_{OP,\max}$ versus R_E

4.5 Effects of heat leakage thermal resistance

It can be noticed from Eq. (20) that the heat leakage thermal resistance R_L has a great influence on cooling capacity, but has rarely been discussed in prior investigations. Figure 11 demonstrates the properties of the coupled system at various values of R_L.

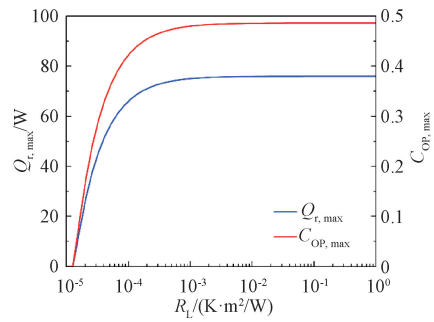

Fig. 11 Curves of $Q_{r,\max}$ and $C_{OP,\max}$ versus R_L

With increasing R_L, both $Q_{r,\max}$ and $C_{OP,\max}$ first increase rapidly and then remain virtually invariant. As R_L increases from 2×10^{-5} K·m^2/W to 1×10^{-3} K·m^2/W, $Q_{r,\max}$ improves from 26.63 W to 75.13 W, and $C_{OP,\max}$ rises from 0.17 to 0.48. As R_L increases from 1×10^{-3} K·m^2/W to 1 K·m^2/W, $Q_{r,\max}$ elevates from 75.13 W to 76.04 W and $C_{OP,\max}$ grows from 0.48 to 0.49. It can be observed that when R_L is low, its variation has a dramatic impact on the system performance. The existence of heat

leakage between external heat reservoirs often leads to a waste of heat, which further significantly deteriorates system performance. In conclusion, for the practical system, enhanced insulation measures between external heat reservoirs are necessary.

4.6 Effects of hot reservoir temperature

To demonstrate the impact of the hot reservoir temperature on the coupled system performance, T_H is varied from 290 K to 310 K. As indicated in Fig. 12, both $Q_{r,max}$ and $C_{OP,max}$ decrease monotonically as T_H increases. To be specific, as T_H rises from 290 K to 310 K, $Q_{r,max}$ diminishes from 120.62 W to 28.54 W, and $C_{OP,max}$ diminishes from 0.81 to 0.18. This is due to the growth in T_H being accompanied by a decline in the temperature span $T_1 - T_H$, which reduces the impetus for external heat transfer. The results demonstrate that increasing T_H always has a positive influence on the properties of systems, and a lower T_H is an effective route to improve overall cooling capacity.

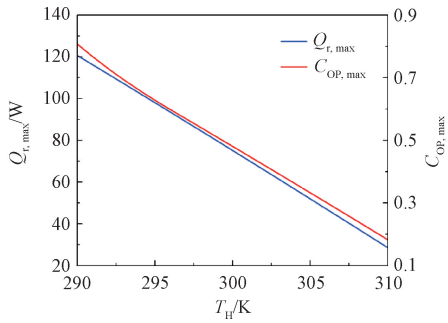

Fig. 12 Curves of $Q_{r,max}$ and $C_{OP,max}$ versus T_H

5 Conclusions

A novel coupled system of a vdWH-based thermionic refrigerator driven by a PV module is developed. Considering the irreversible losses of the system, mathematical expressions for the refrigerating capacity and COP of the coupled system are derived. The general properties of the system are analyzed, and the findings indicate that the maximum refrigerating capacity and the maximum COP are 75.88 W and 0.49, respectively. Besides, the voltage range allowing the coupled system to operate is obtained. Subsequently, detailed parametric investigations are undertaken to evaluate the impact of various work situations and designed factors on the performance of the coupled system. The outcomes illustrate that increasing solar irradiance, inter-layer thermal resistance and heat leakage thermal resistance improve the properties of the coupled system, while rising external thermal resistance and hot reservoir temperature degrade the system performance. The study outcomes may facilitate the establishment and operation of such a novel coupled system.

Furthermore, this paper focuses on the establishment of a numerical model of the novel solar cooling coupled system and theoretically investigates its performance characteristics at a steady state. One point to note is that the theoretical model inevitably has slight errors with the actual system due to necessary simplifications of the real physical processes, assumptions made during the construction of the model, and the difficulty of reflecting the current state of the technology in the calculations. A more comprehensive theoretical model and an associated experimental system need to be developed in future research to facilitate the practical application of coupled systems. And, its performance potential and application value can be further explored in conjunction with environmental effects and economic analysis.

References

[1] PAMBUDI N A, SARIFUDIN A, FIRDAUS R A, et al. The immersion cooling technology: current and future development in energy saving [J]. *Alexandria Engineering Journal*, 2022, 61(12): 9509-9527.

[2] SHARMA G, NARAYANAN K, ADEFARATI T, et al. Frequency regularization of a linked wind-diesel system using dual structure fuzzy with ultra-capacitor [J]. *Protection and Control of Modern Power Systems*, 2022, 7(1): 12.

[3] YANG D Z, KLEISSL J, GUEYMARD C A, et al. History and trends in solar irradiance and PV power forecasting: a preliminary assessment and review using text mining [J]. *Solar Energy*, 2018, 168: 60-101.

[4] KABIR E, KUMAR P, KUMAR S, et al. Solar energy: potential and future prospects [J]. *Renewable & Sustainable Energy Reviews*, 2018, 82: 894-900.

[5] DANANDEH M A, MOUSAVI G S M. Comparative and comprehensive review of maximum power point tracking methods for PV cells [J]. *Renewable and Sustainable Energy Reviews*, 2018, 82: 2743-2767.

[6] ELAVARASAN R M, MUDGAL V, SELVAMANOHAR L, et al. Pathways toward high-efficiency solar photovoltaic thermal management for electrical, thermal and combined generation applications: a critical review [J]. *Energy Conversion and Management*, 2022, 255: 115278.

[7] LAZZARIN R M, NORO M. Past, present, future of solar cooling: technical and economical considerations [J]. *Solar Energy*, 2018, 172: 2-13.

[8] ALLOUHI A, KOUSKSOU T, JAMIL A, et al. Solar driven cooling systems: an updated review [J]. *Renewable and Sustainable Energy Reviews*, 2015, 44: 159-181.

[9] SAIKIA K, VALLÈS M, FABREGAT A, et al.

A bibliometric analysis of trends in solar cooling technology[J]. *Solar Energy*, 2020, 199: 100-114.

[10] DAI Y J, WANG R Z, NI L. Experimental investigation and analysis on a thermoelectric refrigerator driven by solar cells [J]. *Solar Energy Materials and Solar Cells*, 2003, 77(4): 377-391.

[11] CHENG T C, CHENG C H, HUANG Z Z, et al. Development of an energy-saving module via combination of solar cells and thermoelectric coolers for green building applications [J]. *Energy*, 2011, 36(1): 133-140.

[12] ZHAO Q, ZHANG H C, HU Z Y, et al. Performance prediction of a new solar-driven electrochemical refrigerator[J]. *Applied Thermal Engineering*, 2020, 178: 115589.

[13] LONG R, LI B D, LIU Z C, et al. Performance analysis of a solar-powered electrochemical refrigerator[J]. *Chemical Engineering Journal*, 2016, 284: 325-332.

[14] LIAO T J, HE Q J, XU Q D, et al. Coupling properties and parametric optimization of a photovoltaic panel driven thermoelectric refrigerators system [J]. *Energy*, 2021, 220: 119798.

[15] MAHAN G D. Thermionic refrigeration [J]. *Journal of Applied Physics*, 1994, 76(7): 4362-4366.

[16] HISHINUMA Y, MOYZHES B Y, GEBALLE T H, et al. Vacuum thermionic refrigeration with a semiconductor heterojunction structure [J]. *Applied Physics Letters*, 2002, 81(22): 4242-4244.

[17] AÇIKKALP E, YEREL KANDEMIR S, AHMADI M H. Performance evaluation of the thermophotovoltaic-driven thermoionic refrigerator [J]. *Journal of Energy Resources Technology*, 2020, 142(3): 032001.

[18] ZIABARI A, ZEBARJADI M, VASHAEE D, et al. Nanoscale solid-state cooling: a review [J]. *Reports on Progress in Physics*, 2016, 79(9): 095901.

[19] DING Z M, CHEN L G, SUN F R. Performance analysis and optimization of a single-barrier solid-state thermionic refrigerator with external heat transfer[J]. *Heat Transfer Engineering*, 2012, 33(8): 693-703.

[20] SHAKOURI A, BOWERS J E. Heterostructure integrated thermionic coolers [J]. *Applied Physics Letters*, 1997, 71(9): 1234-1236.

[21] MAHAN G D, WOODS L M. Multilayer thermionic refrigeration [J]. *Physical Review Letters*, 1998, 80(18): 4016-4019.

[22] FAN X F, ZENG G H, LABOUNTY C, et al. SiGeC/Si superlattice microcoolers[J]. *Applied Physics Letters*, 2001, 78(11): 1580-1582.

[23] LI J, YANG X D, LIU Y, et al. General synthesis of two-dimensional van der Waals heterostructure arrays [J]. *Nature*, 2020, 579(7799): 368-374.

[24] QIU S S, DING Z M, CHEN L G. Performance evaluation and parametric optimum design of irreversible thermionic generators based on van der Waals heterostructures [J]. *Energy Conversion and Management*, 2020, 225: 113360.

[25] WANG X M, ZEBARJADI M, ESFARJANI K. High-performance solid-state thermionic energy conversion based on 2D van der Waals heterostructures: a first-principles study [J]. *Scientific Reports*, 2018, 8: 9303.

[26] QIU S S, DING Z M, CHEN L G, et al. Performance optimization of thermionic refrigerators based on van der Waals heterostructures[J]. *Science China Technological Sciences*, 2021, 64(5): 1007-1016.

[27] LIANG S J, LIU B, HU W, et al. Thermionic energy conversion based on graphene van der Waals heterostructures [J]. *Scientific Reports*, 2017, 7: 46211.

[28] LIU Y, HUANG Y, DUAN X F. Van der Waals integration before and beyond two-dimensional materials[J]. *Nature*, 2019, 567(7748): 323-333.

[29] ROSUL M G, LEE D, OLSON D H, et al. Thermionic transport across gold-graphene-WSe_2 van der Waals heterostructures [J]. *Science Advances*, 2019, 5(11): eaax7827.

[30] CAI Y, WANG W W, WANG L, et al. A proton exchange membrane fuel cell-compound thermoelectric system: bidirectional modeling and energy conversion potentials [J]. *Energy Conversion and Management*, 2020, 207: 112517.

[31] HUANG Y W, LI D Y, CHEN Z. Potential analysis of a system hybridizing dye-sensitized solar cell with thermally regenerative electrochemical devices[J]. *Energy*, 2022, 260: 125102.

[32] LIAO T J, LIN B H, YANG Z M. Performance characteristics of a low concentrated photovoltaic-thermoelectric hybrid power generation device [J]. *International Journal of Thermal Sciences*, 2014, 77: 158-164.

[33] ZHANG X N, HUANG Y W, CHEN Z. Performance evaluation of an integrated photovoltaic module and cascading thermally regenerative electrochemical devices system[J]. *Energy Conversion and Management*, 2022, 264: 115737.

[34] LE PIERRÈS N, COSNIER M, LUO L G, et al. Coupling of thermoelectric modules with a photovoltaic panel for air pre-heating and pre-

cooling application; an annual simulation [J]. *International Journal of Energy Research*, 2008, 32(14): 1316-1328.
[35] ZHANG X N, HUANG Y W, CHEN Z. A hybrid system integrating photovoltaic module and thermoelectric devices for power and cooling cogeneration[J]. *Solar Energy*, 2022, 239: 350-358.
[36] CHEN X G, HUANG Y W, CHEN Z. Energy and exergy analysis of an integrated photovoltaic module and two-stage thermoelectric generator system[J]. *Applied Thermal Engineering*, 2022, 212: 118605.
[37] ZHAO Q, ZHANG H C, HU Z Y, et al. A solar driven hybrid photovoltaic module/direct contact membrane distillation system for electricity generation and water desalination [J]. *Energy Conversion and Management*, 2020, 221: 113146.
[38] CHEN L G, DING Z M, SUN F R. Performance analysis of a vacuum thermionic refrigerator with external heat transfer [J]. *Journal of Applied Physics*, 2010, 107(10): 104507.
[39] LIANG S J, ANG L K. Electron thermionic emission from graphene and a thermionic energy converter[J]. *Physical Review Applied*, 2015, 3: 014002.
[40] SATA Y, MORIYA R, MORIKAWA S, et al. Electric field modulation of Schottky barrier height in graphene/$MoSe_2$ van der Waals heterointerface [J]. *Applied Physics Letters*, 2015, 107(2): 023109.
[41] Suniva optimus ® series monocrystalline solar modules [EB/OL]. (2018-05-25) [2023-04-01]. https://unboundsolar.com/1524436/suniva/solar-panels/suniva%02opt285-60-4-100-silver-mono-solar-panel.
[42] SACHENKO A V, KRYUCHENKO Y V, KOSTYLYOV V P, et al. Temperature dependence of photoconversion efficiency in silicon heterojunction solar cells: theory vs experiment [J]. *Journal of Applied Physics*, 2016, 119(22): 225702.
[43] WU S Y, ZHONG Z H, XIAO L, et al. Performance analysis on a novel photovoltaic-hydrophilic modified tubular seawater desalination (PV-HMTSD) system[J]. *Desalination*, 2021, 499: 114829.
[44] SEME S, ŠTUMBERGER B, HADŽISELIMOVIČ M, et al. Solar photovoltaic tracking systems for electricity generation: a review[J]. *Energies*, 2020, 13(16): 4224.

光伏模块驱动的基于范德华异质结构的热离子制冷器的性能评估

鹿 振, 黄跃武*
东华大学 环境科学与工程学院, 上海 201620

摘 要: 为了开发高效的太阳能冷却技术, 建立了一个由光伏 (photovoltaic, PV) 模块和基于范德华异质结构 (van der Waals heterostructure, vdWH) 的热离子制冷器 (thermionic refrigerator, TIR) 组成的新型耦合系统。在充分考虑内部和外部的不可逆因素的情况下, 建立了耦合系统的理论模型, 推导了关键性能指标的数学表达式。在此基础上, 研究了耦合系统的一般性能特征, 并确定了允许系统运行的电压区域。根据计算, 最大制冷量和最大性能系数 (coefficient of performance, COP) 分别为 75.88 W 和 0.49。此外, 还进行了灵敏度分析, 以得出关键参数对整体性能影响的规律和大小, 包括太阳辐照度、有效肖特基势垒高度、层间热阻、外部热阻、热泄漏热阻和热库温度。所得结果可能有助于实际耦合系统的设计和运行。

关键词: 光伏 (PV) 模块; 热离子制冷器 (TIR); 范德华异质结构 (vdWH); 耦合特性; 灵敏度分析